SAND2019-1361J

An Experimental and Numerical Study of the Scattering Properties of Ice Crystals with Black Carbon Inclusions

Marco Arienti[1], Manfred Geier[2], Xiaoyuan Yang[3], John Orcutt[4], Jake Zenkert[4], Sarah D. Brooks[4]

Abstract

This paper focuses on the optical properties of ice crystals when they nucleate on atmospheric black carbon (BC). The parameters examined in this study are the shape of the ice crystal, the volume fraction of the BC inclusion, and its location inside the crystal. We report on new spectrometer measurements of forward scattering and backward polarization from ice crystals seeded by BC particles and grown under laboratory-controlled conditions. Data from the Cloud and Aerosol Spectrometer with Polarization (CASPOL) are used for direct comparison with single-particle calculations of the Mueller phase matrix. Geometrical optics and discrete dipole approximation techniques are jointly used to provide the best compromise of flexibility and accuracy over a broad range of size parameters. Together with the

[1] Sandia National Laboratories, Livermore, CA.
[2] Independent Scholar, Albany, NY
[3] The Climate Corporation, San Francisco, CA.
[4] Department of Atmospheric Sciences, Texas A&M University, College Station, TX.

interpretation of the trends revealed by the CASPOL measurements, the numerical results confirm previous reports on absorption cross-section magnification, even in the case of complex crystal shapes. They also offer new insights on the relation between relative position of the BC inclusion with respect to the crystal outer surfaces, the shape of the crystal, and its size.

1. INTRODUCTION

The aerosol direct effect is the radiative forcing that results from both enhanced backscattering and absorption of solar radiation by atmospheric aerosol. The challenge in predicting the radiative forcing of compound aerosol particles depends on how its different components are combined. At one extreme, each aerosol component can be assumed to be physically separated from the others components, therefore creating an external mixture of chemically pure modes. At the other extreme, the aerosols can be assumed to be internally mixed in the limit of a homogeneous material reflecting the chemical and physical average of all the contributing components. This question becomes particularly pressing when ice crystals nucleate on atmospheric soot, specifically the small, very dark particles resulting from combustion henceforth referred to as black carbon (BC). The determination of the mixing rules for ice-BC particles is important because BC is the dominant light-absorbing aerosol particle, with positive radiative forcing (warming) in the atmosphere (Ramanathan & Carmichael 2008, Bond *et al.* 2013). In ice-BC particles the dominant absorption contribution of BC is largely confined to wavelengths shorter than about 1.4 μm, beyond which ice absorption predominates.

Much of the analysis of the absorption enhancement factor for isolated hydrometeors has been carried by treating the compound particle as a compact, spherical core surrounded by a mixed shell (Ackerman and Toon, 1981). In weakly-absorbing spheres,

radiation is focused near the center, enabling absorption enhancement if absorbing inclusions reside near the center of the composite (Flanner et al., 2012). For instance, Jacobson (2012) included a coat of secondary organic aerosol to the BC core (at 40, 80, or 120 nm diameter) and calculated the absorption cross-section of the resulting core-shell particle, finding an enhancement ratio between two and four with respect to the pure BC core. The annually-averaged aerosol coefficient ratio of internal mixing of BC with respect to external mixing was estimated to be 2.4. In reality, soot particles may have open, chainlike shapes even after being surrounded by organic matter and can be located in off-center positions within their host materials. Such embedded soot absorbs sunlight less efficiently than when it is compact and located near the center of its host particle (Adachi et al., 2010). Cappa *et al.* (2012) compared measurements of particle absorption enhancement from two field campaigns in California with results from average mixing states from core-shell (CS), concluding that the CS model overestimated measured values by approximately a factor of two.

An additional cause of uncertainty is due to the shape of the atmospheric ice crystals (Kaufman *et al.* 1994). Spheroidal or cylindrical approximations are often assumed, amongst others by Mishchenko & Sassen (1998), Lee *et al.* (2003), and Nicolet *et al.* (2012); a broader population of regular hexagonal columns, plates, droxtals, hollow columns and bullets was examined by Bi & Yang (2014). But in the airborne data collected using the Cloud Particle Imager (Korolev *et al.* 1999), only 3% of the particles were in “pristine” shape, that is, regular column, needle, plates and dendrites geometries. The remaining 97% of crystals were either irregular faceted polycrystallines, sublimating ice particles with smooth curving sides and edges, or aggregates of columns and plates (Heymsfield & Iaquinta 2000; Yang *et al.* 2013). Microscale surface roughness, included through stochastic models with assumed distribution of crystal face tilt angles, is also

found to affect the evaluation of ice radiative effects, in particular the asymmetry factor (Geogdzhayev and van Diedenhoven, 2016). Finally, the size of atmospheric ice crystals exhibits a strong spatial and temporal variability, as shown for instance by data from the International Cirrus Experiment (ICE) or by the First International Satellite Cloud Climatology Project (ISCCP) Regional Experiment (FIRE; Kinne *et al*. 1997). Data collected from these campaigns are typically fitted to a set of assumed shapes, but the variability of ice crystals shape, size and BC volume fraction is not precisely known.

The approach taken in this work is different in that ice crystals are grown in laboratory from soot particles, under controlled temperature, humidity and flow conditions; the spectrometry data obtained at these conditions are then compared with single-particle parametric calculations from models that take into account the crystal shape and the BC location. In a previous study, the Cloud and Aerosol Spectrometer with Polarization (CASPOL), manufactured by Droplet Measurement Technologies, was used to evaluate the optical scattering signatures of dust particles (Glen and Brooks, 2013). The spectrometer was placed at the exit of an ice nucleation chamber (the Continuous Flow Diffusion Chamber, or CFDC – Glen and Brooks, 2014) and mineral dusts were introduced to act as ice nuclei (IN). In the work reported here, BC particles of reproducible size are used as nuclei.

On the computational side, the discrete dipole approximation (DDA) and the ray tracing (RT) technique are used to account for the effects of an arbitrary crystal shape and BC location. When the characteristic length D of the particle is smaller than the incident wavelength, scattering is rather insensitive to shape, that is, when the size parameter $X = \pi D/\lambda > 1$ only the largest-scale deviations from the spherical shape may be significant (e.g., Nousiainen et al., 2001). As X increases, the geometrical details of the particle become important. For wavelength-scale compound particles, the internal

inclusion description becomes more relevant and justifies using a volume-integral method, such as DDA. At sufficiently large size parameters ($X > 500$), scattering becomes increasingly sensitive to shape, making geometrical optics (or RT) techniques appealing.

In the range of size parameters between approximately 50 and 500, the need to explicitly account for wavelength-scale particle details while the particles themselves are considerably larger than the wavelength is a well-known modeling challenge. This remains a difficult territory to explore (e.g., Nousiainen, 2009), although the numerically exact Invariant-Imbedding T-Matrix (II-TM) method (Bi et al., 2013) promises to bridge that gap. One of the tests presented here consists of a direct comparison between the phase matrices derived from ADDA and RTMCX for $X = 50$.

In the first part of the paper, the comparison of the scattering signal from CASPOL is carried out to assess the relevant trends in crystal shape. This comparison is not trivial because of the uncertainty in the crystal shape and the noise in the back-scattered signal. With the computational tools so established, we carry out parametric studies to try and separate the effects due to BC volume fraction, inclusion position, and shape of the ice crystal.

2. BC INCLUSION MODEL AND CRYSTAL SHAPES

Crystallization of water in the atmosphere occurs through homogenous freezing of liquid droplets or through heterogeneous nucleation processes facilitated by atmospheric particles that act as ice nuclei (IN) (Vali, 1985). The heterogeneous nucleation of interest in this work occurs through a variety of freezing modes, including those in which ice grows from water vapor (deposition mode) or from a supercooled liquid water droplet (Hoose and Mohler, 2012; Murray et al., 2012, Fornea et al., 2009).

After being emitted, BC particles coagulate to form aggregates or chain-like structures consisting of hundreds or thousands of spheres (Lahaye & Ehrburger-Dolle 1994; Schwarz *et al.* 2006). The morphology of the aggregate structures evolves in time ("aging") in a manner that is very relevant to the optical characteristics of soot (Chen *et al.* 1990). The possibility that multiple BC aggregates are contained inside a single ice particle could be quite high, but in first approximation we assume that the BC material is all contained into a spherical core. The BC core mimics a dense aggregate of monomers, whose individual diameters are smaller than the wavelength. While inclusions can even touch the surface if the crystal, it is important to point out that in this work they are always assumed in its interior.

An example of this modified Core-Shell (CS) approach is illustrated in Figure 1. There the crystal shape is the regular hexagonal prism with the two parameters, external diameter D and length L. The parameters D and L will vary, determining different aspect ratios (AR=L/D), as well as the core diameter D_p and its position inside the crystal.

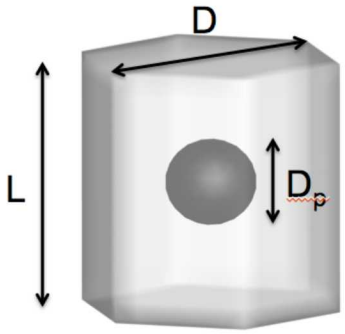

Figure 1 Example of modified Core-Shell inclusion model.

A similar inclusion model, with spherical bubbles sized according to a prescribed distribution inside a hexagonal prism, has been recently adopted by Hong and Minnis

(2015) in their analysis of the single-scattering properties of small ice crystals containing ammonium sulfate, ammonium nitrate and air bubbles in addition to BC.

More complex crystal shapes can be obtained by the combination of Voronoi cells generated from an assigned fractal dimension. Recent studies have shown that empirical correlations between the effective diameter and the mass of retrieved atmospheric crystals would be more in agreement with fractal-based shapes than with simpler geometries (Ishimoto et al., 2012). A single Voronoi cell is has a convex shape and is displayed in Figure 2 (left) together with an example of cell assemblage (right), not necessarily convex. The geometrical properties of these shapes can be made to mimic the process of formation by conglomeration of a falling crystal following the observations by Schmitt and Heymsfield (2010).

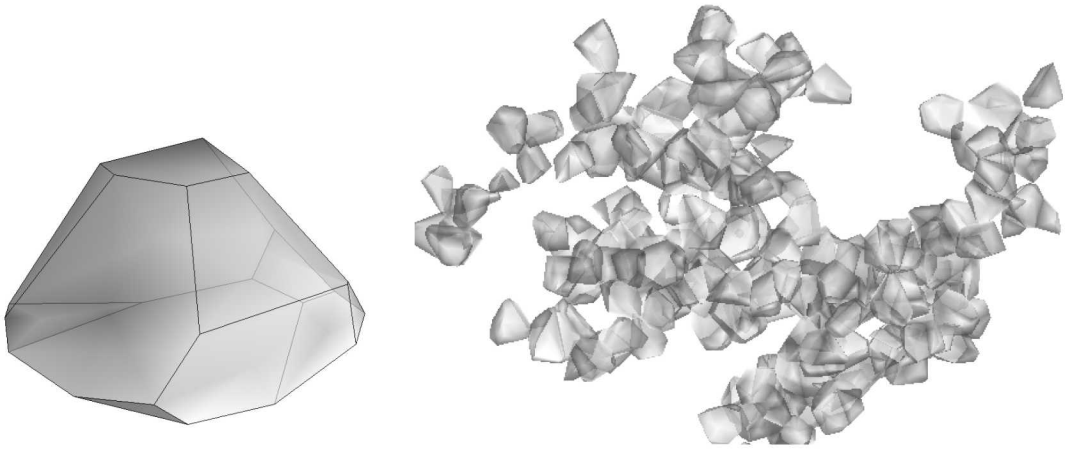

Figure 2. Single Voronoi cell and assemblage of cells.

Both convex and not convex shapes will be considered in the analysis that follows, although the parametric studies will essentially concern regular prisms of varying aspect

ratios. Finally, the real (n_r) and imaginary (k_r) refractive indices of BC used in this work are expressed as function of wavelength (λ, in microns) as

$$n_r = 2.0248 + 0.1263 \log \lambda + 0.027 \log^2 \lambda + 0.0471 \log^3 \lambda$$

$$k_r = 0.7779 + 0.1213 \log \lambda + 0.2309 \log^2 \lambda - 0.01 \log^3 \lambda \quad (1)$$

in the range 0.3-5.0 μm (Flanner et al. ,2012). In this same range, the refractive index of ice is set to 1.3117 + 0i (Kokhanovsky, 2013).

3. TECHNIQUES OF OPTICAL ANALYSIS

3.1. The discrete dipole approximation - ADDA

In this well-known approach, the volume of the scatterer is divided into small cubical sub-volumes, or dipoles, which interact with each other and the incident field. The resulting internal field, or its direct derivative, polarization, is solved by matrix inversion. The specific implementation of the DDA used in this work is the Amsterdam Discrete Dipole Approximation (ADDA) by Yurkin & Hoekstra (2013). Orientation averaging is carried out on the three Euler angles (α, β, γ) that specify the particle orientation with respect to the laboratory reference frame. In ADDA, the rotation over α, equivalent to rotating the scattering plane without changing the orientation of the scatterer relative to the incident radiation, does not demand additional computational cost (Yurkin & Hoekstra 2013, Della Sala & D'Agostino 2013). Averaging over the remaining two angles requires instead numerical integration over a discrete set of pairs (β, γ), performed by Romberg

integration (Davis & Rabinowitz 2007). Because ADDA runs on multiprocessor systems using the Message Passing Interface protocol, the turnaround time for orientation averaging calculations can be substantially reduced. A comparison of the overall performance of four different DDA codes – ADDA, DDSCAT, SIRRI and ZDD – is reported by Penttilä *et al.* (2007).

3.2. Geometrical optics - RTMCX

The size of most ice crystals within cirrus clouds may be of the order of several tens or hundreds of microns, placing the corresponding size parameters inside the geometric optics regime when the solar spectral region is analyzed. BC inclusions, however, introduce smaller scales and therefore the need to capture internal diffraction. The Monte-Carlo ray tracing (RTMC) code (Macke 1993, Macke *et al.* 1996, Macke *et al.* 1996b) was modified to enable the specification of the locations of spherical inclusions within the crystal. This modification (called RTMCX), developed at Sandia National Laboratories, permits to evaluate the effect of position of any number of small internal scatterers on the overall optical properties of the compound particle. While the original RTMC used a specified free-mean path and a random number to determine the distance between internal extinction events, RTMCX relies on user-specified extinction cross-sections that define a circular “collision” cross-section for the ray. Scattering properties of the inclusions are pre-calculated (from Mie theory if the inclusions are spherical) and stored in a table that is accessed at run time. Following the procedure outlined in Muinonen *et al.* 2009, when a ray encounters an inclusion the two angles defining the direction of the scattered ray are determined in a Monte Carlo procedure from the specified angular distribution of

scattered intensities and from the polarization state of the ray incident on the inclusion. The complete phase matrix is determined for each internal scatter.

The RTMCX solution procedure involves tracking the Stokes vectors of collected light in both azimuthal and polar angle bins for four different incident polarization states. Rays collected in the same angle bin are superposed, provided that the polarization state (Stokes vector) of the causing incident ray is the same. For a particular scattering direction (ϑ, ϕ), the relationship between the Stokes vectors of the incident rays and the emerging rays can be expressed as

$$(\boldsymbol{I}_1, \boldsymbol{I}_2, \boldsymbol{I}_3, \boldsymbol{I}_4)_{sca}(\vartheta, \varphi) = \boldsymbol{P}(\vartheta)\boldsymbol{L}(\varphi)(\boldsymbol{I}_1, \boldsymbol{I}_2, \boldsymbol{I}_3, \boldsymbol{I}_4)_{inc} \ , \tag{2}$$

where $\boldsymbol{I}_j$ is the Stokes vector corresponding to the *j*-th incident Stokes vector (in column notation). The unknown phase matrix $\boldsymbol{P}(\vartheta)$ follows by solving the linear system of equations $\boldsymbol{Y} = \boldsymbol{PX}$, where $\boldsymbol{Y}$ is a 4-by-4*n* matrix composed of the 4-by-4 matrices for each polar angle ϕ and $\boldsymbol{X}$ is the corresponding matrix compiled from rotated incident Stokes vectors $\boldsymbol{X} = \boldsymbol{L}(\phi)(\boldsymbol{I}_1, \boldsymbol{I}_2, \boldsymbol{I}_3, \boldsymbol{I}_4)_{\text{inc}}$ (the definition of the rotation matrix $\boldsymbol{L}(\phi)$ can be found in Mishchenko *et al.* 2002). Under the assumption that the phase matrix has the structure of randomly oriented particles, the 10 independent phase matrix elements of $\boldsymbol{P}$ are determined by linear regression, $\boldsymbol{P} = \boldsymbol{YX}^{\dagger}(\boldsymbol{XX}^{\dagger})^{-1}$. Next, assuming that the observed Stokes vectors are random variables with equal variances, the uncertainties in the estimated phase matrices are computed. The output is a valid Mueller matrix that is calculated for each scattering angle ϑ by the eigen-decomposition of the coherency matrix (Hovenier *et al.,* 1996). Results are valid only in the large size parameter limit: the extinction efficiency is hard-wired to the limit value of two (Bohren et al., 1983).

4. MODEL VERIFICATION

4.1. RTMCX and Mie scattering theory

The first verification test for RTMCX is the comparison of the calculation for a large homogenous sphere with the results from Mie-scattering theory (described, for instance, in Mishchenko et al., 2002). The size parameter of this test was X = 10000 and the refractive index of the scatterer was m = 1.3117 + i0.0. The Mie solution was averaged over 1° angle intervals to match the angle bins used by the ray tracing software. The sphere was approximated by a polyhedron with 36, 1088, and 10224 triangles. The RTMCX simulations used 1000, 100, and 10 random orientations for the approximations with 36, 1088, and 10224 faces, respectively (1000 rays were used for each orientation).

As expected, the plots of the nonzero elements in Figure 3 show that the agreement with the analytical solution improves with the increasing number of faces, in particular at scattering angles less than 90°. The angular dependence of the element Z_{11} was captured even for scattering angles reaching far backwards to about 170°, which is remarkable given the variation of Z_{11} by over four orders of magnitude. The other nonzero elements Z_{12}, Z_{22}, Z_{33}, Z_{34}, and Z_{44}, relative to Z_{11}, were less closely captured and exhibited larger local variability. This variability can be attributed to insufficient coverage due to the sparsity of the Monte Carlo sampling.

Overall, RTMCX calculations with 1088 and 10244 faces yielded less than 1% deviation of total scattering cross-sections and asymmetry factors with respect to the analytical values; using 36 faces caused relative errors of 15% and 6% for the total scattering cross section and the asymmetry factor, respectively.

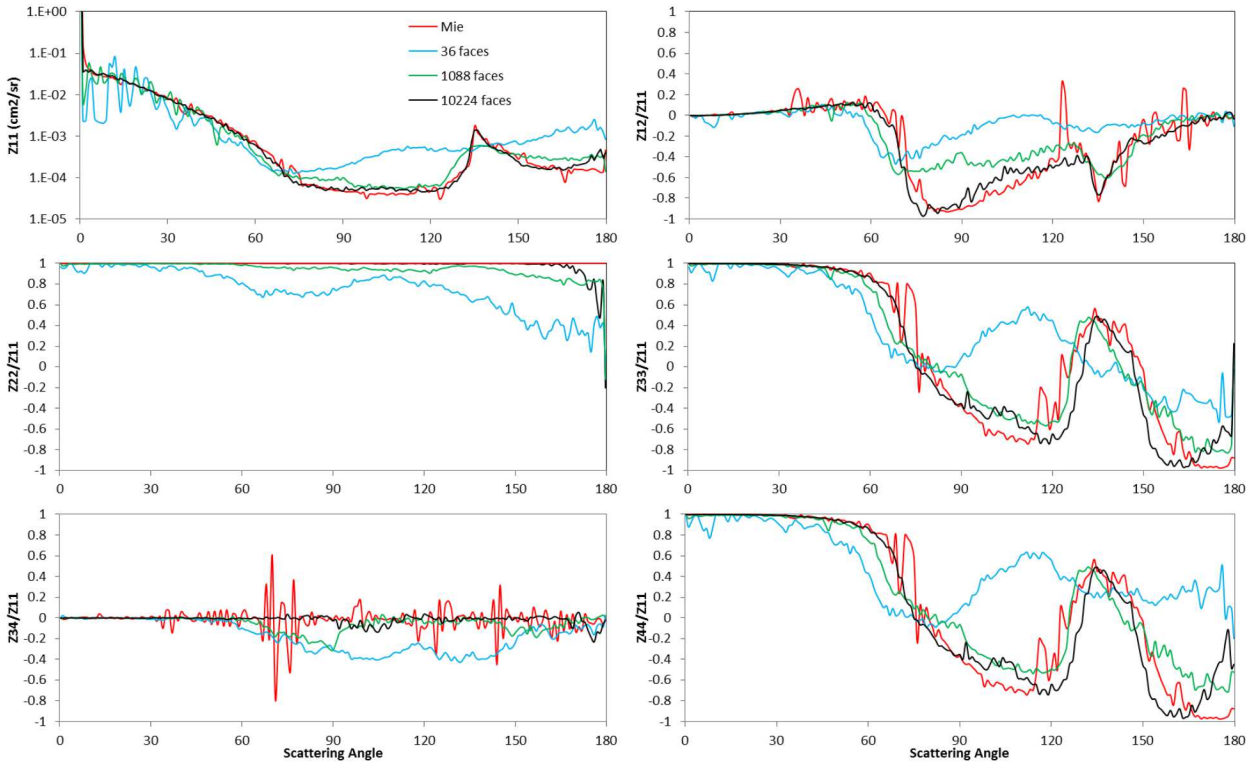

Figure 3. Nonzero elements of the scattering phase matrices for a large sphere. The reference phase matrix from the analytical solution (Mie, red line) is compared with the RTMCX elements obtained from a tessellation of the sphere with 34, 1088 and 10234 faces.

4.2. RTMCX and ADDA

A second test consists in the direct comparison between the phase matrices derived from ADDA and RTMCX. This test is challenging because the assumptions of geometrical optics start loosing validity when the size parameter is smaller than 500, whereas the DDA matrix inversion begins to have difficulty converging when the size parameter is larger than 10. In the case of the hexagonal prism shape, the maximum size parameter for which we could achieve a complete ADDA calculation was $X = 50$ for a pure ice crystal

with L/D = 1, D = 9.79 μm, λ = 660 nm. The computationally intensive β- and γ-averaging operations needed to be carried out with a small number N of orientation evaluations, N = 129. Therefore, instead of a sequence of random number pairs, two pseudo-random sequences of Halton numbers (β_i, γ_i) $i = 1 \ldots N$ where used (the Halton sequence typically provides a better sampling than purely random sampling, see Penttil and Kumme (2011)). The quadrature convergence rate was increased by using as weights the values of the areas A_i corresponding to the Voronoi tessellation on a unit sphere: $\omega_i = A_i/(4\,\pi)$.

The matrix elements Z_{13}, Z_{14}, Z_{23}, Z_{24}, Z_{31}, Z_{32}, Z_{41}, and Z_{42} average to zero regardless of the scattering angle because of the symmetry properties of the hexagonal prism (Mishchenko *et al.* 2000). The angular distributions of the scattering phase matrix elements from ADDA and from RTMCX are shown in Figure 4: the match between the two curves is fairly good. Looking more closely at the plot of Z_{11}, we see that ray tracing recovers the two ice halos at 22° and 46° (Bohren et al., 1983). These features may be exaggerated, as suggested by the comment of Macke and Mishchenko (1999) that well-defined halos should not be prevalent for size parameters less than 100; Bi *et al.* (2014) also suggest that ice halos from geometric optics are too prominent for a size parameter as large as 120. The two halos are greatly smoothed in the ADDA results, although some of the smoothing may also be caused by ADDA's approximation of sharp edges through dipoles.

The values of the scattering parameters are listed on Table 1: note that the scattering efficiency for ADDA is Q_{ext} = 1.3 (C_{ext} = 122.4) compared to the fixed limit value of 2 for RTMCX.

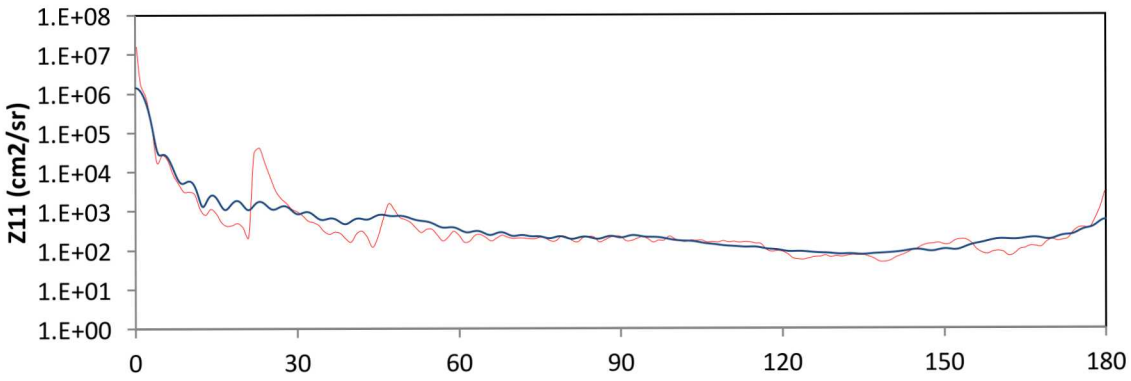
Z11 (cm2/sr)
1.E+08
1.E+07
1.E+06
1.E+05
1.E+04
1.E+03
1.E+02
1.E+01
1.E+00
0
30
60
90
120
150
180

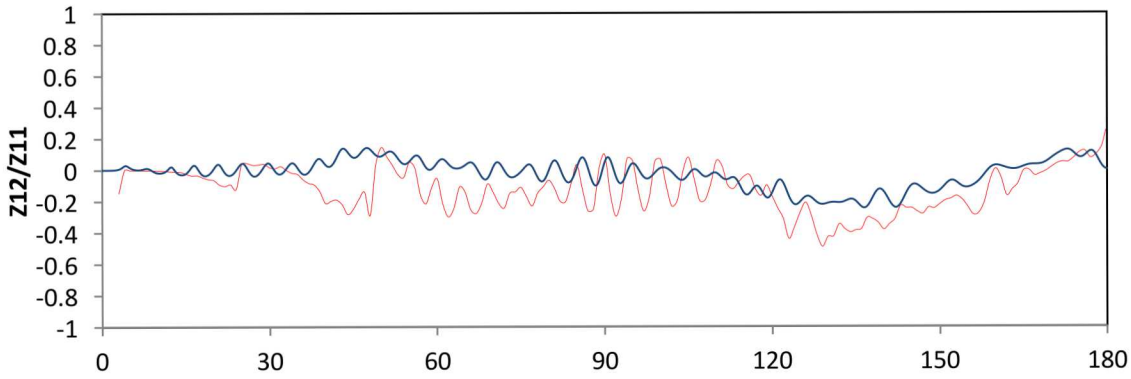
Z12/Z11
1
0.8
0.6
0.4
0.2
0
-0.2
-0.4
-0.6
-0.8
-1
0
30
60
90
120
150
180

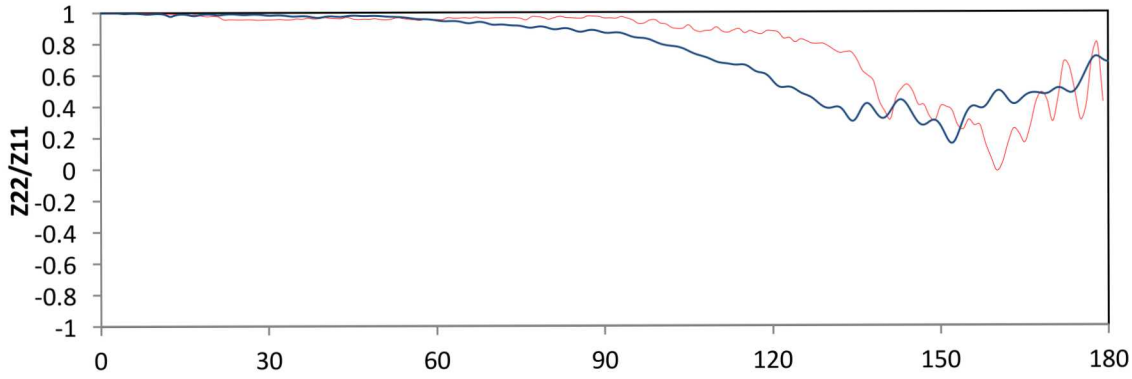
Z22/Z11
1
0.8
0.6
0.4
0.2
0
-0.2
-0.4
-0.6
-0.8
-1
0
30
60
90
120
150
180

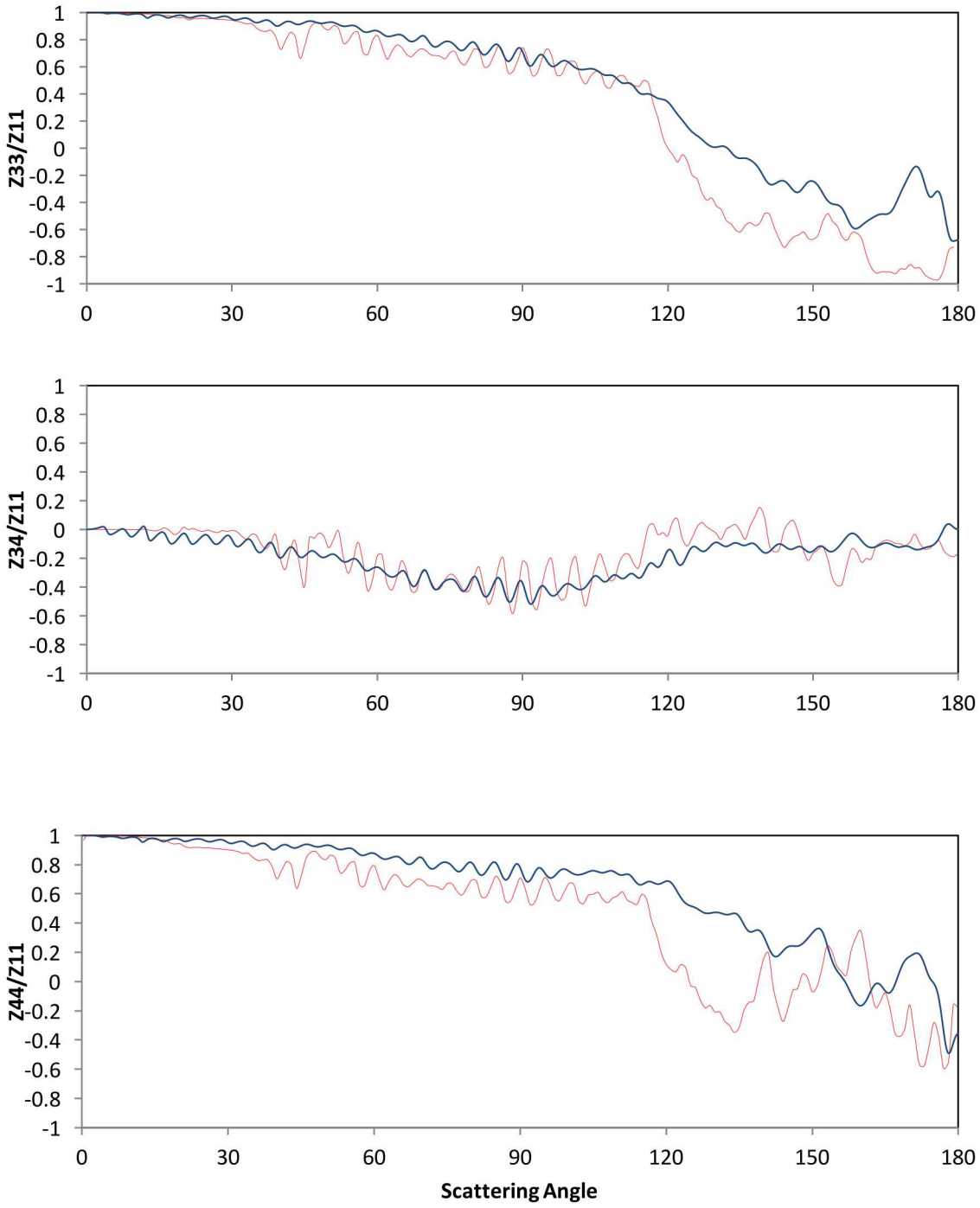

Figure 4 Comparison ADDA - RTMCX: angular distribution of scattering phase matrix elements for randomly oriented hexagonal pure ice crystals with L/D = 1, D = 9.79 μm, λ =

660 nm, refractive index m_{ice} = 1.3117 + i0.0. Red lines: RTMCX output; blue lines: ADDA output. The phase function is expressed in log 2.

Table 1. Comparison of discrete dipole and ray tracing approach for the same pure ice hexagonal prism with random orientation.

	ADDA	RTMCX
Q_{abs}	0.3206	0.426
Q_{ext}	1.298	2
C_{abs} [μm^2]	27.66	44.8
C_{ext} [μm^2]	112.0	206

5. VALIDATION: COMPARISON WITH CASPOL MEASUREMENTS

The Cloud and Aerosol Spectrometer with Polarization (CASPOL), manufactured by Droplet Measurement Technologies, is a rather unique measurement tool in that it can measure optical properties of individual particles. The CASPOL features a detector to measure light scattered in the near-forward direction and two detectors for polarization-specific measurement of light scattered in near-backward direction. A beam of light with 680 nm wavelength illuminates a particle that moves through the probe volume and produces the scattered light for detection. In forward direction, the instrument measures light scattered in the spherical segment between 4° and 12° from the beam propagation direction (forward scattering intensity, FSI); in the backward direction, two separate detectors simultaneously measure parallel and perpendicular polarized light scattered in

the spherical segment between 168° and 176°. Application of three different gain stages that cover the required wide dynamic range of the signals in the near-forward direction enables analysis of particles from 0.6 µm to 50 µm in size.

The factory calibration of CASPOL forward detection line was verified by injecting droplets of olive oil/isopropanol suspensions. As described by Glen and Brooks (2013), spherical olive oil droplets with controlled diameter were generated with a Vibrating Orifice Aerosol Generator, by TSI, Inc.. The large-size channel of the forward scattering diagnostics (7.9 µm to 50 µm) and the two backscattering channels were verified with 10 µm to 17 µm olive oil droplets. Calibration of the small-size and medium size channels of the forward scattering diagnostics was not possible as the droplet generator failed to reliably generate oil droplet sizes less than 8 µm. Our analysis thus concentrates on the ice crystals with a water-equivalent droplet size of 7.9 µm and larger.

Establishing a calibration constant for the polarization-sensitive backscattering detectors required several steps. As the instrument reports the diameter of a water droplet that produces the same signal in the near-forward detector for each olive oil droplet detected, the first step is to convert this water-equivalent diameter to an actual oil drop diameter, which in turns allows for prediction of the corresponding signals in the backscattering detectors. Weakly absorbing droplets (such as water and olive oil droplets) produce forward scattering intensities related to the droplet diameter through a non-monotonic, oscillatory relationship in the investigated size range (size parameters are between 36 and 230). As the instrument employs a 10-point monotonic FSI-to-diameter mapping, a correlation was established for the olive oil droplets in order to enable 1:1 conversion between scattering-equivalent oil and water droplet sizes (the refractive index of olive oil at λ = 680 nm was assumed to be 1.46). The uncertainties in the converted oil droplet diameters are around 1.4 µm (the root mean squared deviation from theoretical

predictions obtained with the Mie-scattering code *bhmie*, Bohren et al., 1983). After estimation of the oil droplet diameter from the forward-scattering intensities, the corresponding theoretical backscattering signals were calculated and related to the detector signals in order to establish the calibration constants necessary for correct specification of polarization ratios.

The expected CASPOL signals were determined from the polarization state of the incident beam, $\boldsymbol{I} = (1,1,0,0)^t$, the scattering phase matrix, $\boldsymbol{P}$, and the transmission Mueller matrix of the polarizer, $\boldsymbol{T}$ (Bohren et al., 1983) by integrating over the solid angle subtended by the detectors. Other invariable parameters, such as geometric dimensions, transmissivities, electronic gains, and the intensity of the incident beam were lumped into a constant. The transmission characteristics of optical components other than polarizers were assumed to be insensitive to the polarization state of the transmitted light.

As the CASPOL is configured to collect light over the full azimuthal (φ) angle range, the FSI for an arbitrary particle is given by

$$FSI \propto (1,0,0,0)^t . \left(\int_0^{2\pi} \int_{4^\circ}^{12^\circ} \boldsymbol{L}(-\varphi) . \boldsymbol{P}(\vartheta, \varphi) . \boldsymbol{L}(\varphi) . \boldsymbol{I} \sin(\vartheta) d\vartheta d\varphi \right) \quad (3)$$

where $\boldsymbol{L}$ is the rotation matrix defined in Mishchenko *et al.* 2002. For a spherical particle of size d_P this expression simplifies to

$$FSI(d_P) = k_F \int_{4^\circ}^{12^\circ} P_{11}(d_P, \vartheta) \sin(\vartheta)\, d\vartheta \quad (4)$$

where k_F is a proportionality factor that needs to be established by comparison of the theoretical expression with the signal magnitude of the near-forward detector.

The signals in the detectors for light polarized parallel and perpendicular with respect to the scattering plane are similarly obtained from

$$BSI_{\parallel,\perp} \propto (1,0,0,0)^t . \boldsymbol{T}_{\parallel,\perp} . \left(\int_0^{2\pi} \int_{168^\circ}^{176^\circ} \boldsymbol{L}(-\varphi) . \boldsymbol{P}(\vartheta,\varphi) . \boldsymbol{L}(\varphi) . \boldsymbol{I} \sin(\vartheta) d\vartheta d\varphi \right) \tag{5}$$

which, for spherical scatterers, simplifies to

$$BSI(d_P)_\parallel = k_\parallel \int_{168^\circ}^{176^\circ} \left[P_{11}(d_P,\vartheta) + \tfrac{1}{2}\left(P_{22}(d_P,\vartheta) + P_{33}(d_P,\vartheta) \right) \right] \sin(\vartheta)\, d\vartheta, \tag{6}$$

$$BSI(d_P)_\perp = k_\perp \int_{168^\circ}^{176^\circ} \left[P_{11}(d_P,\vartheta) - \tfrac{1}{2}\left(P_{22}(d_P,\vartheta) + P_{33}(d_P,\vartheta) \right) \right] \sin(\vartheta)\, d\vartheta. \tag{7}$$

Note that for spherical particles $P_{11}(d_P,\vartheta) = P_{22}(d_P,\vartheta)$, so that the ratio of the backscattering polarization signals (referred to as in-situ depolarization ratio (DR) in Glen and Brooks (2013)) reduces to

$$\frac{BSI(d_P)_\perp}{BSI(d_P)_\parallel} = \frac{k_\perp \int_{168^\circ}^{176^\circ} [P_{11}(d_P,\vartheta) - P_{33}(d_P,\vartheta)] \sin(\vartheta)\, d\vartheta}{k_\parallel \int_{168^\circ}^{176^\circ} [3P_{11}(d_P,\vartheta) + P_{33}(d_P,\vartheta)] \sin(\vartheta)\, d\vartheta} \tag{8}$$

This ratio remains greater than zero regardless of the particle diameter. Consequently, both polarization-sensitive channels can be calibrated on the basis of detected scattered light from (sufficiently large) spherical droplets.

While simplifications for spherical particles do not apply to individual non-spherical shapes, the signal equations hold for an ensemble of randomly oriented scatterers that consists of randomly located mirror-symmetric particles present in equal numbers. The

combined scattered intensity in that case is equal to the sum of intensities from each particle. The average of the CASPOL signals from a sufficiently long sequence of probed particles thus converges to signals that would be produced by the phase matrix elements P_{11}, P_{22}, and P_{33}. This property enables meaningful comparison of data from the CFDC-CASPOL with predictions of our simulations with the RTMC and ADDA codes, which provide the orientation-averaged phase matrix elements of single ice-crystals with BC inclusions. Note that the CASPOL integrates out one orientation angle owing to its optical configuration; each particle is, however, not monitored long enough during its flight through the probe volume to provide a truly orientation-averaged signal. For the results discussed below we conservatively report only the average intensities (or the water-equivalent drop diameters). Although the CFDC-CASPOL collects single particle measurements, more than 300 particles were averaged for most of the conditions intensities .

5.1. Measurements of ice crystals nucleated on soot particles

The procedure to nucleate ice crystals onto soot is briefly explained in the following. A modified Santoro-type laminar diffusion burner (Santoro et al., 1983) was used to generate the soot particles by incomplete combustion of propane. The soot generator consisted of two concentric tubes; a 66 mm i.d. outer tube with a ceramic laminar flow element on top, where the air went through, and a 7 mm i.d. inner tube where the propane flowed through (Khalizov et al., 2009). A glass cylinder above the burner acted as chimney to protect the flame from outside influences. The flow rates were ~1.7 L min^{-1} for the airflow and ~0.75 mL min^{-1} for the propane flow. Typical flames extended 7-10 cm from the top of the inner tube. An inlet, approximately placed 6 cm above the top of the flame,

directed particles to a differential mobility analyzer (DMA) which size-selected soot particles with diameters of 50, 100, or 200 nm in diameter. Size-selected aerosols from the DMA were directed to the CFDC-CASPOL.

An inlet at the top of the CFDC allowed the pre-generated aerosol stream to enter an annular chamber where the sample air was sandwiched between two laminar flows of dry filtered air. The walls of the chamber were coated with ice and held at different temperatures so that a highly controlled supersaturation field could be established. As the soot particle traveled through this controlled supersaturation region, it nucleated and formed ice. The crystal growth conditions for four experiments are listed in Table 2; because of the generation procedure, the soot particle is assumed to be approximately located at the center of each crystal. The resulting ice crystals arriving in the CASPOL range in size from 1 to 45 microns; their shape, however, is not exactly known because it is controlled by many parameters, including temperature and supersaturation conditions. With reference to Table 2, we note that the crystal growth conditions for Sample 1 are substantially different from those of the other three samples, even though the soot diameters for Samples 1 and 2 were both 50 nm in diameter. We will discuss this point later.

Table 2. Crystal growth conditions

Sample	Soot Diameter	SS Water	SS Ice	Temperature Outer Wall	Temperature Inner Wall	Aerosols Location Temp.
1	50 nm	27.6 %	118 %	-20.6 C	-56.3 C	-55.0 C
2	50 nm	92 %	264 %	-65.0 C	-27.0 C	-41.4 C
3	100 nm	131 %	216 %	-65.0 C	-27.0 C	-38.7 C
4	200 nm	42.0 %	255 %	-65.0 C	-27.0 C	-42.3 C

5.2. Comparison of results for BC-ice composites

The forward scattering signals from the four outputs of the CASPOL are plotted in Figure 5. The signal intensities show a rapid increase up to approximately 2 μm, followed by a more moderate increment up to 10 μm, and eventually by what appears to be a plateau. Importantly, we observe that the volume fraction of the BC inclusions in the measured crystal size range is too small to noticeably affect the scattering signals in both forward and backward scattering signals.

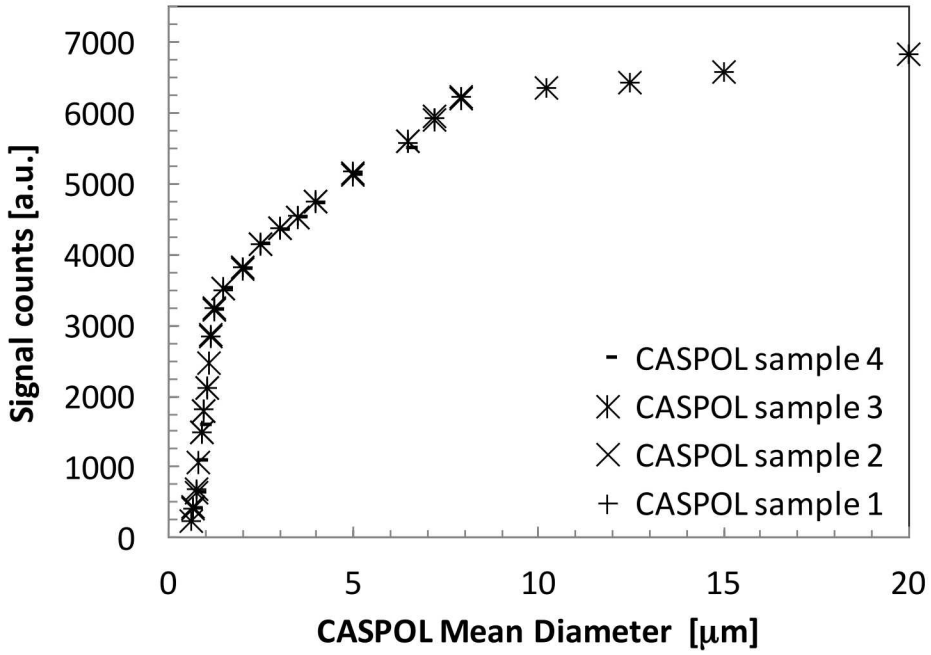

Figure 5. Forward detector signal counts from CASPOL binned by calibrated size.

The insensitivity to the BC diameter is confirmed by a set of calculations carried out with ADDA (for volume-equivalent sphere diameters smaller than 3 μm) and with RTMCX (for larger diameters). The assumed shapes in those calculations were regular hexagonal

prisms with different aspect ratios. The results are plotted in Figure 6. Also shown (as a green line) is the limit case of a perfectly spherical crystal, obtained from the coated Mie model following Bohren *et al.* 1983 (implemented in a Matlab script by Mätzler, 2004); the line is calculated by keeping the core BC diameter constant while increasing the diameter of the shell.

We observe that:

- The initial ramp-up of the CASPOL signal is in agreement with basic coated Mie theory.
- By and large, ADDA and RTMC results agree in the size range where they overlap.
- Total scattering cross sections for the crystals agree well with the predictions for volume equivalent spheres.
- The forward signals deviate from the signals for volume-equivalent spheres for larger crystals; this is due to the shift of scattered light in the 4°-12° range to the halo peaks at larger angles. A spherical diameter calculated from 4°-12° scattering measurements would largely under-represent the total scattering cross section of that crystal.
- Among ice crystals, the aspect ratio appears to have little effect on forward signal (consistent with the measured scattered intensity); the backward parallel scattering signal is more sensitive to shape. But it is also possible in some cases that the fluctuations of the RTMCX results (each obtained using 1000 rays and 100 orientations) are too large to accurately detect particle shapes.

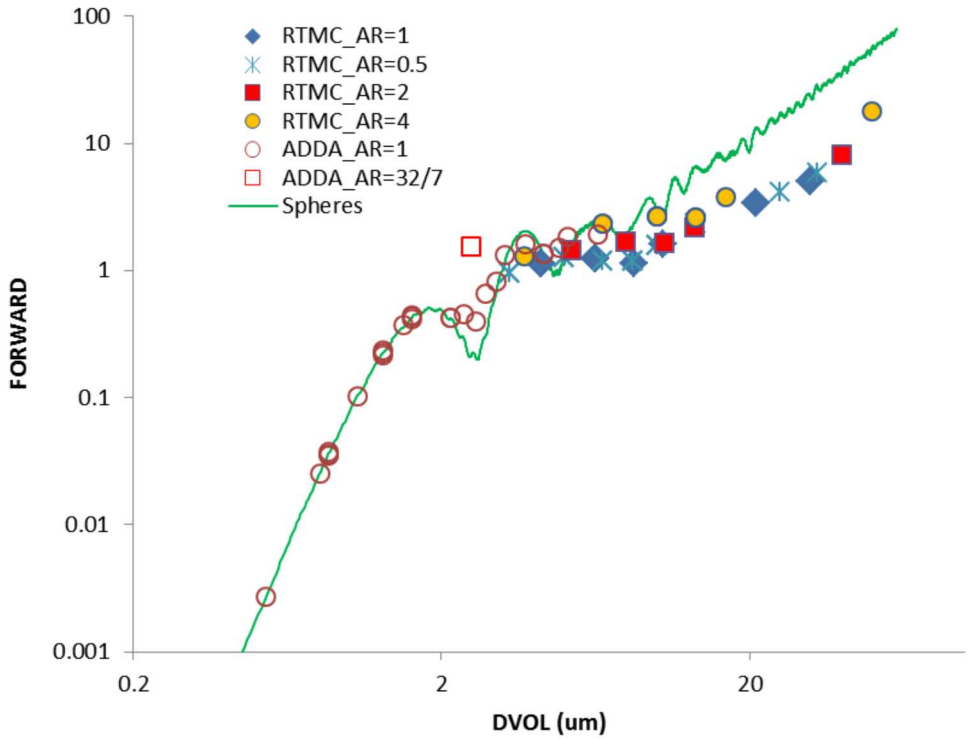

Figure 6. Calculated forward scattering signal (per unit radian azimuthal angle) from integration of Z_{11} over the polar angle between 4° and 12°. DVOL is the diameter of the volume-equivalent sphere.

To establish a characteristic crystal size and shape for each experimental condition, the averages of the measured scattering intensities needs to be evaluated. This mimics the conditions of ensemble measurements, where a large number of particles is illuminated to produce a composite scattering signature of the particulate. On the other hand, a direct comparison of simultaneously measured forward and polarization-sensitive backward scattering signals with orientation-averaged calculations would not be particularly meaningful, as a CASPOL measurement in our setting is practically a snapshot of the crystal in a particular orientation.

The four experimental conditions of Table 2 can each be represented by a point at the corresponding water-equivalent diameter of the samples. This is shown in Figure 7 for the parallel-polarized backward scattered light and in Figure 8 for the perpendicular-polarized backward scattered light. As in the previous diagram, simulation results from ADDA and RTMCX are overlaid to display the qualitative agreement with the measured signals. Based on the distribution of the experimental points in both diagrams, it would seem that larger crystals were formed on smaller BC particles, Moreover, supersaturation was lower for Sample 1 than for Sample 2, yet the generated crystals are larger than those of Sample 2. A possible explanation is that the residence times for Sample 1 were longer due to overall lower temperatures of the gas flow, which would cause lower superficial velocities and thus possibly increase the time for crystal growth before the detection in the CASPOL. Further experiments at more controlled conditions will be necessary to rule out this possibility. Because the growth conditions (and presumably the residence times) were similar for Samples 2 to 4, the measured data provide reason to believe that larger BC nuclei give rise to smaller crystal sizes. This conjecture is substantiated by the fact that the number of particles larger than 7.9 μm (the calibrated size range) dropped from over 800 for Sample 2 (50 nm BC) to 19 for Sample 3 (100 nm BC) and to 1 for Sample 4 (200 nm BC).

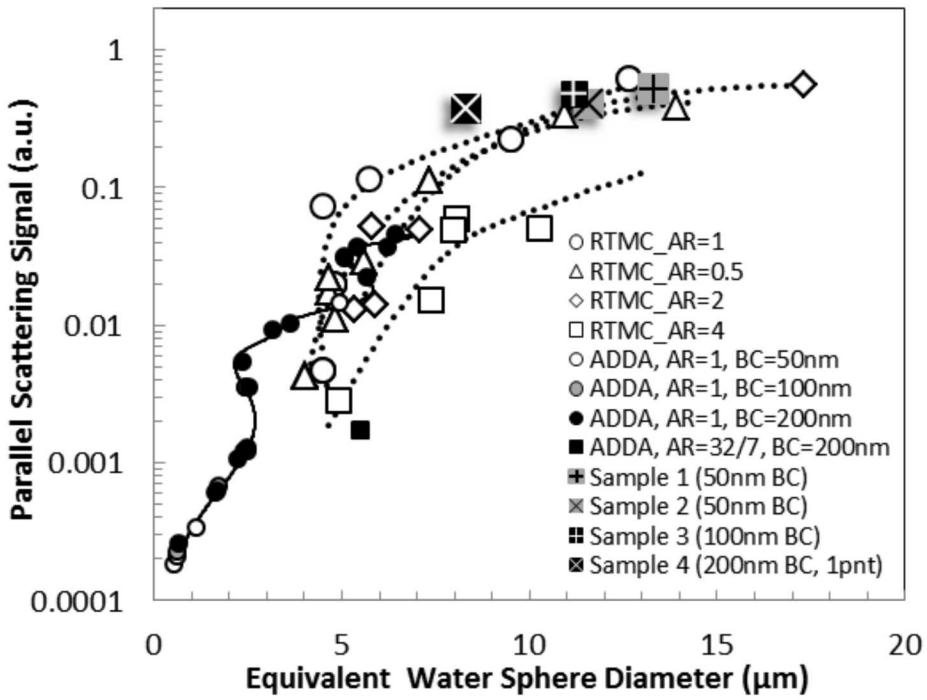

Figure 7. Parallel Backscatter Signal vs. Equivalent water drop diameter (converted from forward signal). Simulation results from ADDA: solid circles; from RTMCX: open symbols; experimental data: X-ed and crossed square symbols.

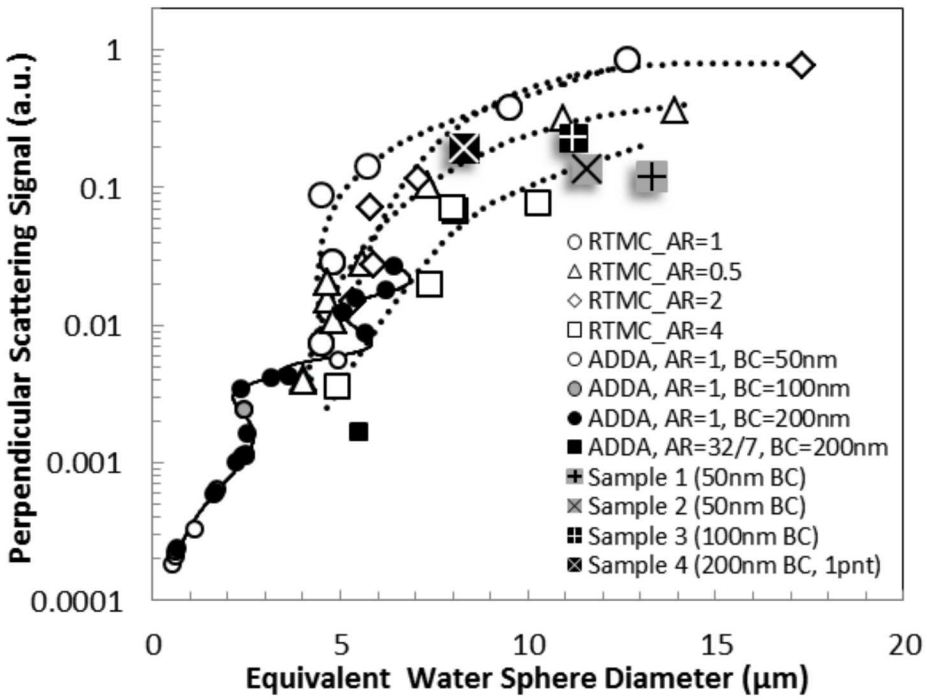

Figure 8. Perpendicular Backscatter Signal vs. equivalent water drop diameter (converted from forward signal). Simulation results from ADDA: solid circles; from RTMCX: open symbols; experimental data: X-ed and crossed square symbols.

As far as the crystal shape is concerned, the parallel-polarized backscattering signal magnitudes are well within the range of the RTMCX predictions for crystals with aspect ratios around unity (Figure 7). While parallel scattering signals could suggest that BC diameter plays a minor role in detecting the crystal shape, the perpendicular-polarized backward scattering signals paint a different picture (see Figure 8). For the observed sizes, the signals calculated with RTMCX are similar for particles with aspect ratios around 1 to 2, but smaller for particles outside of that AR range. The observed perpendicular scattering intensities for all samples could therefore stem from particles with aspect ratios less than 1 or larger than 2. Particles with aspect ratios less than 1, i.e. plate-like crystal shapes, are overall more consistent with the parallel scattering signals.

Thus, one possible interpretation of the diagram in Figure 8 is that the the crystals that generated the backscattering signals had aspect ratios that increased from less than 0.5, for 50 nm BC, to around 1, for 200 nm BC nuclei.

Clearly more data are necessary to solidify these conclusions, but at this point we suggest that the size of soot particles may play a role in determining both size and morphology of ice crystals that nucleate on the soot particles. If this hypothesis is correct, soot particles would indirectly affect the distribution of light scattered by ice crystals in the atmosphere in addition to directly affecting the radiative energy balance as a broadband absorber.

At this stage we can conclude that CASPOL data provide information on both particle size (through the less shape-sensitive forward scattering signal) and on crystal shape (through the backscattering signals or the polarization ratio). Thus, for the same volume-based diameter, differences in signal can be attributed to the crystal shape, provided the particle is illuminated long enough for random orientation to be a reasonable assumption. In the remaining of this paper we therefore address some of the aspects of the complex interaction between crystal shape and BC inclusions using the numerical tools described in the first part. Thanks to the consistency between geometrical optics and discrete dipole approximation, when necessary in our analysis we will assume we can seamlessly switch from one to the other.

6. PARAMETRIC ANALYSIS

6.1. Effects due to BC volume fraction

We first assess the effect of BC volume fraction on the cross-section magnification, defined as the ratio between the absorption cross-section of the BC-ice compound and

the absorption cross-section of the BC sphere in air (the absorption cross section of the pure ice crystal is taken to be zero). In the following parametric study, the diameter of a hexagonal prism of AR=1 is varied from 9.79 μm to 195 μm, while keeping a centered black carbon sphere inclusion of diameter D_p = 6.15 μm. The absorption cross-section of the BC sphere in air is C_{abs} = 30.3 μm^2 (35.71) at λ = 0.660 μm. The results from a set of RTMCX calculations (for size parameter X =πD/λ = 500 or larger) are shown in Figure 9a as a function of the BC volume fraction.

The same information is re-arranged in Figure 9b by taking the minimum distance between the sphere surface and the hexagonal prism surface normalized by wavelength. In both plots a definitive trend can be recognized: the cross-section magnification is independent from the actual BC volume fraction as long as this is sufficiently small. In this case we recover the result that the absorption of the compound particle increases by about 75%, as reported by Flanner et al. (2012). But the magnification decreases if the volume fraction increases above 5%, which suggests a decreased effectiveness of the ice crystal as a “lens”. This result can be explained by looking at Figure 9b: the cross-section magnification decreases if the embedded BC becomes sufficiently close to the crystal’s outer surface.

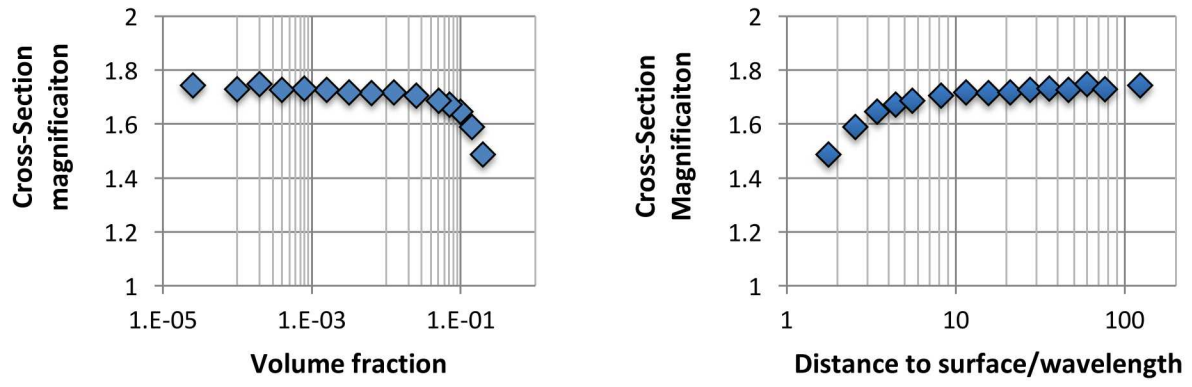

(a) (b)

Figure 9. Magnification of the absorption cross-section of a compound particle with fixed BC location and diameter but varying crystal volume. (a) magnification vs. BC volume fraction; (b) magnification vs. smallest distance between the BC sphere and the crystal surface.

6.2. Effects due to BC position

The variation in cross-section magnification noted in the previous plots can be re-examined by parameterizing the inclusion position while keeping constant the size of the hexagonal prism (D = L = 97.9 μm) and the size of the inclusion (D_p = 6.15 μm). The BC sphere can take any random position along the crystal's z-axis. The result is illustrated in Figure 10, where the absorption cross-section of the compound particle is plotted as a function of the normalized distance to the crystal surface, corresponding to different positions of the BC sphere. Also reported in the plot is the 95% confidence interval, estimated as the standard deviation from five RTMCX calculations multiplied by the t-factor 2.57. In this case too, we find that magnification factor is 1.7 and that the magnification decreases when the gap between the BC sphere and the crystal face is less than 10 λ.

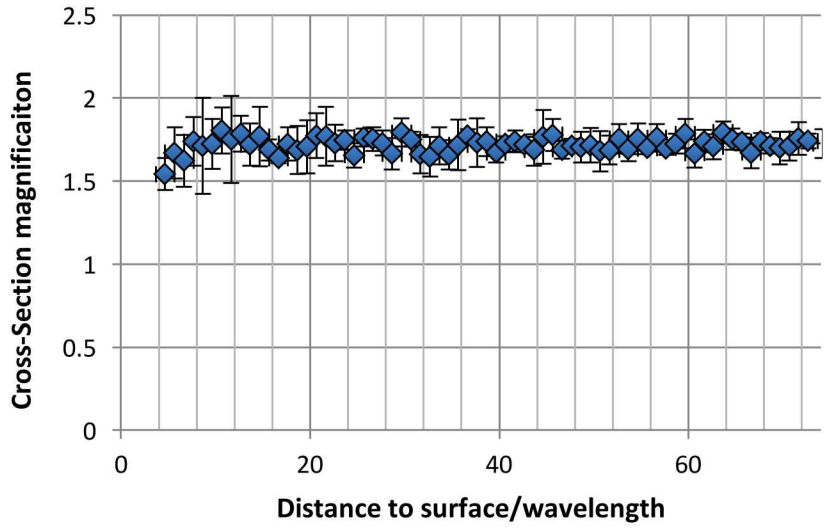

Figure 10. Absorption cross-section vs. BC distance from the crystal surfaces with fixed BC diameter and crystal shape. Error bars represent 95% confidence intervals derived from 5 RTMCX calculations (100 orientations with 100 rays per orientation).

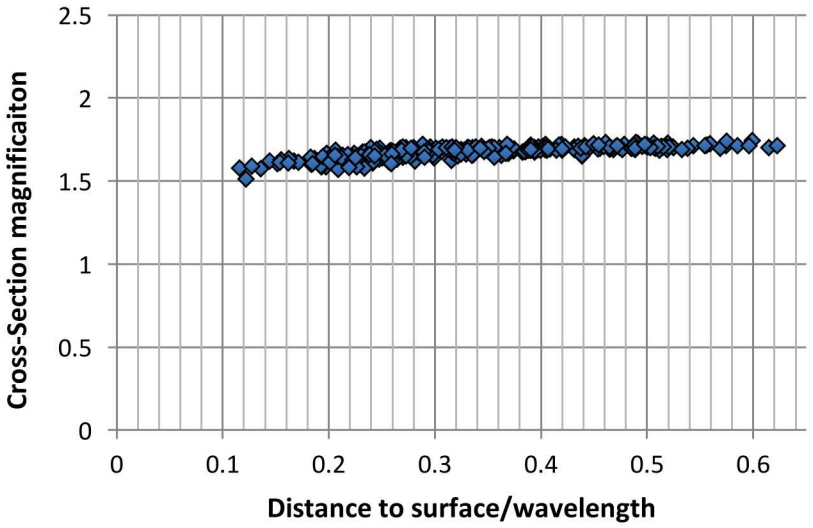

Figure 11. Cross-section magnification effect from 300 ADDA sample calculations parameterized by the position of the BC insertion.

The RTMCX calculations above are intrinsically limited by the minimum distance the inclusion can be placed with respect to the external surfaces of the scatterer; ADDA provides a complementary view of the magnification effect when the distance of the BC particle is comparable or smaller than the wavelength. In Figure 11, the BC inclusion is allowed to take any position inside the crystal, as long as the sphere is completely contained inside the prism, for a total of 300 independent samples. In this set of calculations, D = L = 0.8508 μm (this relatively small value of X enables many calculations in a short period of time) and D_p = 0.21 μm (there is a variation of about 1.4% of the actual volume of the sphere because of the discretization of the spherical shape with cubic dipoles). The maximum available distance to the crystal surface is $d/\lambda = \sqrt{3}/4 \cdot D/\lambda = 0.692$ with λ = 0.532 μm. Consistently with our previous results, the cross-section magnification decreases from 1.75 to a value slightly above 1.5 in the limit case of the BC sphere almost touching the crystal surface. This is quite a remarkable result since it is obtained using crystal and BC particle diameters that are one or two orders of magnitude smaller than their respective values in the previous example. In both cases, the off-center position of the inclusion does not completely eliminate absorption enhancement.

6.3. Effects of crystal shape

We can now begin to differentiate the above observations based on the crystal's shape. For a given volume of ice, the previous results would suggest that crystals with larger surface area reduce absorption efficiency because the inclusions are more likely to end up near the crystal surface. As shown next, this effect may be offset by a higher efficiency of intercepting a beam of light and channeling it to an absorbing particle. It has been previously shown that the variation of the asymmetry factor versus the aspect ratio

presents a distinctive “V-pattern” (Neshyba *et al.* 2003; Grenfell *et al.* 2005; Fu 2007), with the minimum near the unit aspect ratio. For pure crystals, Yang and Fu (2009) systematically analyzed the effect of aspect ratio on the asymmetry parameter and attributed it to the collimated rays that transmit through two parallel faces and propagate along the incident direction.

Figure 12 is a scatter plot of the absorption and scattering efficiencies for four AR values (0.3, 1, 3, 4 and 5) generated by ADDA for small particles (with volume 0.4 μm^3); for each aspect ratio 300 realizations of the BC position were generated by a random uniform distribution. All the efficiencies in ADDA are calculated by dividing the particle’s cross-section by the area of the geometrical cross-section of the sphere having the volume of the dipole representation of the particle. The points are colored by the value of the closest distance from the prism sides, normalized by the wavelength (here, λ = 532 nm). From the diagram, the scattering efficiency increases as the aspect ratio decreases; there is also a minor additional variation due to the position of the inclusion inside the crystal each values of AR. The absorption efficiency exhibits a larger excursion for a given shape, approximately 7-12%, and as previously observed, it increases from the smallest to the largest possible distance to the prism sides. Within the variation due to the inclusion position, the absorption efficiency increases more substantially when AR = 5 and 4, followed by AR = 0.3, 3, and finally 1. Because the crystal volume is maintained constant, the largest minimum distance between the inclusion and the crystal faces is indeed obtained when L = D.

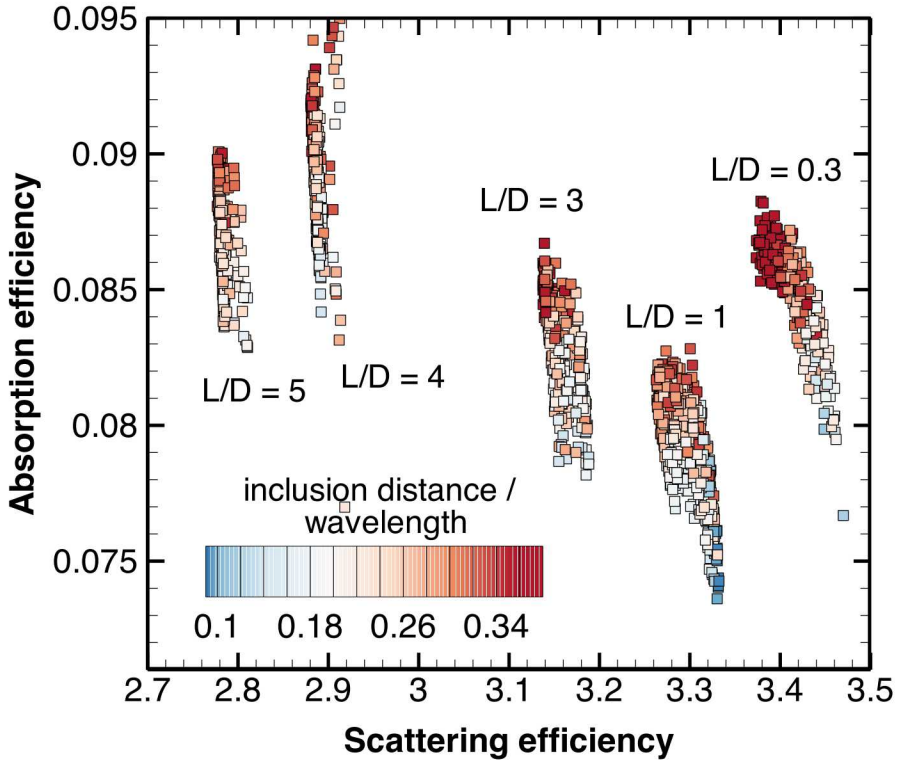

Figure 12. Absorption vs. scattering efficiency: a single BC sphere (of 0.21 μm in diameter) is located at random locations (300 in total) inside a small hexagonal prism of ice with volume 0.4 μm^3. Symbols are colored according to the minimum distance between the center of the BC inclusion and the sides of the ice crystal, normalized by wavelength.

The absorption magnification study is extended in Figure 13 to a broad range of BC volume fractions between $4 \cdot 10^{-7}$ and $2 \cdot 10^{-2}$, and to different crystal shapes at $\lambda = 0.660$ μm. This is accomplished by using a combination of the Mie model for coated spheres, RTMCX and ADDA, depending on the applicable range. As before, the absorption cross-section values are normalized by the corresponding cross-section of the BC sphere in air.

The inclusion is always located in the center of the crystal; depending on its diameter, it can be interpreted as either a single monomer or a compact aggregate.

For perfectly spherical crystals we consider two cases: small and large inclusion diameter. For D_p = 0.05 μm, the values obtained from the Mie model oscillate between an upper and a lower envelop line at or above a magnification value of 2; only these two curves are plotted, as dashed lines, in Figure 13, whereas the actual magnification curve is not shown to avoid cluttering. For a larger inclusion diameter, D_p = 0.308 μm, the magnitude of the magnification oscillations and their average value decrease significantly: the curve is shown as a smooth, continuous line at a magnification of approximately 1.6.

The ADDA calculations (full symbols in Figure 13) and cover the volume fraction range above 10^{-3}. Starting from the volume of the L=D hexagonal prism of 0.1 μm^3, different aspect ratios are obtained by increasing or decreasing L while keeping fixed D. Since the fixed inclusion diameter is D_p = 0.1 μm, the normalized distance of the BC center to the cristal faces is $d/\lambda < 1$.

The RTMCX calculations (empty symbols in Figure 13) cover volume fractions smaller than 10^{-3}. Besides hexagonal prisms, randomly generated individual Voronoi shells (Figure 2) and their aggregates are considered. Aggregates are organized in elongated crystals (square symbols) or in shapes that are closer to spheres (lozenges); D_p = 0.616 μm for the hexagonal prisms and D_p = 6.16 μm for the Voronoi cells (single or aggregate). In all the ray tracing calculations, $d/\lambda > 10$.

All the data points from Figure 13 indicate that absorption magnification is substantial, of the order of 60% or more. While this effect appears not to strongly depend on volume fraction, as pointed out previously, within each data set there are differences that depend on shape. In particular, individual Voronoi cells, near-spherical aggregates, and hexagonal prisms with AR close to unity show a magnification of 1.7, similarly to Mie

spheres with D_p = 0.308 μm; elongated aggregates and prisms have a larger absorption cross-section, of two or more, together with Mie spheres with D_p = 0.05 μm. In the set of hexagonal prisms, the rod-like and plate-like shapes display the largest increase in cross-section, with AR = 10 reaching 2.2; the L=D shape has the lowest. This trend of larger magnification ratios for elongated crystals is reversed in the sub-micrometer domain: there, the magnification is the largest for AR = 1 and 2, because those shapes offer the greatest possible distance d/λ. Conversely, it decreases for L = 0.7D, 0.4D and 0.3D because d/λ becomes smaller.

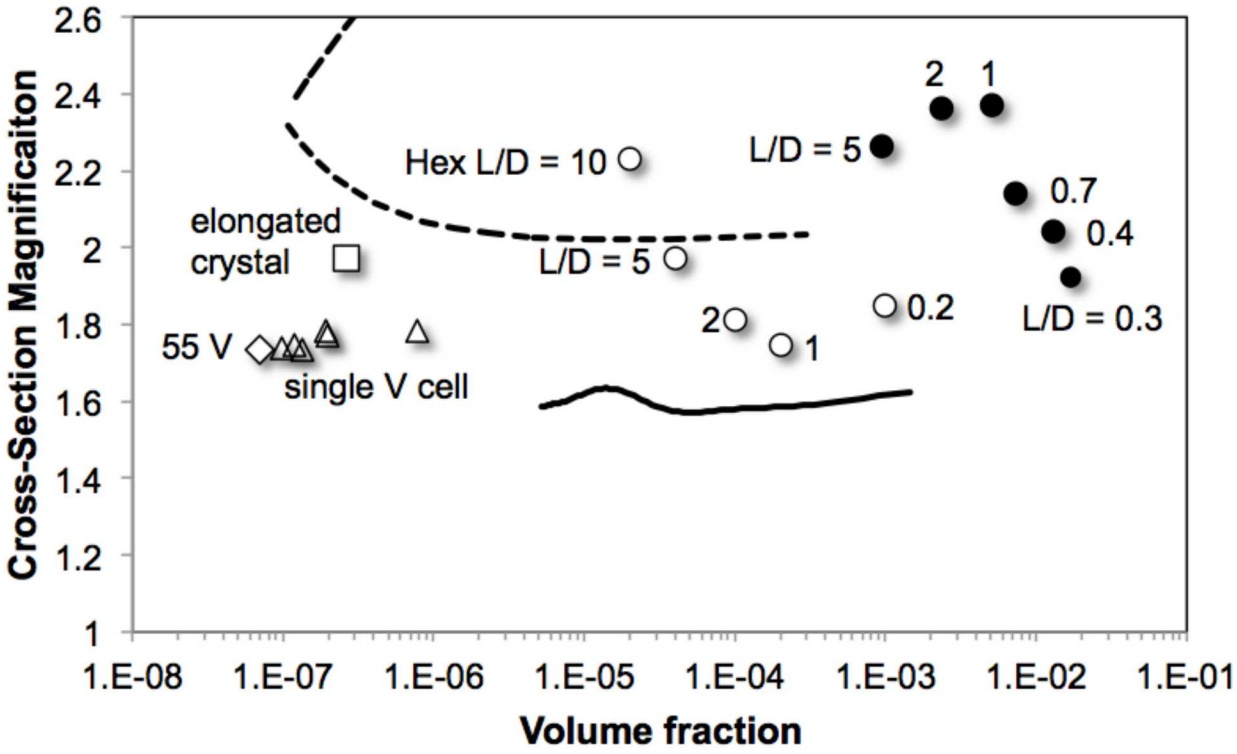

Figure 13. Cross-section magnification of absorption vs. BC volume fraction for representative shapes and aspect ratios of the ice crystal, assuming centered inclusions. See text for explanation.

7. CONCLUSIONS

The study of the radiative properties of BC-ice atmospheric particles is made particularly challenging by the variability of the crystal shapes and the soot inclusion modes; by the scale range between embedded and embedding particles; and by the substantially different absorbing properties of BC compared to ice in the visible range. The experimental procedure presented in this paper indicates a path for determining the scattering properties of ice crystals seeded by BC particles in a controlled environment. The CASPOL measurements indicate that the forward scattering intensity is a strong function of the crystal size while the depolarization ratio of the backscatter signal is weakly dependent on the size of the BC inclusion. A result that requires further investigation is that, based on the parallel-polarized, backward-scattered CASPOL signal, larger crystals seem to form on smaller BC nuclei.

The CASPOL signals were directly compared with the results obtained from a simplified BC inclusion model using the discrete dipole approximation and ray tracing techniques; overall good qualitative agreement was found. Where the sensitivity to the unknown crystal shape in the experiment was stronger, a series of calculations for regular hexagonal prisms was carried out over a range of aspect ratios. For small BC inclusions (50 nm) we found that the perpendicular-polarized, backward-scattered signal was closer to the value calculated for low aspect ratios (plates); for larger BC inclusions (100 and 200 nm), the signal was closer to the value from the AR=1 hexagonal prism. Clearly more data are necessary, but at this point it would seem that the size of soot particles may play a role in determining both size and morphology of ice crystals that nucleate on the soot particles. If this hypothesis is correct, soot particles would indirectly affect the distribution

of light scattered by ice crystals in the atmosphere in addition to directly affecting the radiative energy balance as a broadband absorber.

In the second part of the paper we examined the absorbing properties of ice-BC particles by means of parametric studies based on the BC volume fraction, position and type of crystal shape. Besides spheres and regular hexagonal prisms with varying aspect ratio, random agglomerates of Voronoi cells were used as an instance of crystals generated by a random diffusion-dominated process. A broad range of particle's volumes, from 0.1 to 10^5 μm^3, and seven orders of magnitude in BC volume fraction were covered. Our findings are listed as follows:

- The absorption enhancement is not strongly dependent on the BC volume fraction, as long as this is sufficiently small: 0.1% or less, which may be common in atmospheric ice.
- Absorption enhancement does not strongly depend on the position of the BC monomer or agglomerate, as long as this is sufficiently removed from the crystal's surfaces (of the order of ten times the probing wavelength). Even in the case of inclusions close to the crystal's surface, the absorption enhancement is not completely neutralized.
- Particles that are more elongated provide more absorption for the same volume of ice and BC.
- However, if the ice crystal size is sufficiently small to compare with the wavelength, then the BC volume fraction directly affects the absorption magnification.
- Particularly, in the case of small crystal volumes the dependence on the crystal's aspect ratio tends to be reversed: crystals that are closest to a spherical shape are also the ones that offer the largest available distance of BC from the crystal surfaces.

In summary, in the numerical study of the optical properties of ice-BC aerosol particles the actual crystal shape introduces a substantial variability in the composite particle's absorption, but confirms a lower bound of 1.7 in absorption magnification for centered inclusions, according to the definition adopted here. This value may decrease to 1.5 because of the off-center position of the inclusion, as long as it is completely located inside the crystal. Conversely, because of the exact spherical symmetry implied in the model, predictions by Mie scattering theory oscillate between much broader ranges, depending on volume fraction, and are more sensitive to the BC diameter.

We conclude by noting that, as computationally intense as it was, our numerical analysis is still incomplete. For instance, it did not track changes in the spatial structure of atmospheric soot due to photochemical aging nor include the optical modifications caused by organic matter when it surrounds BC. Additional variability in the results could be caused by roughness of the crystal surfaces and by the possibility that soot and organic matter aggregate outside of the crystal surface. These conditions are identified as future directions of investigation.

8. ACKOWLEDGEMENTS

The guidance by Dr. Macke in using his code RTMC is gratefully acknowledged.

This work was supported by the Laboratory Directed Research and Development program at Sandia. Sandia National Laboratories is a multimission laboratory managed and operated by National Technology and Engineering Solutions of Sandia, LLC., a wholly owned subsidiary of Honeywell International, Inc., for the U.S. Department of Energy's National Nuclear Security Administration under contract DE-NA-0003525.

9. REFERENCES

Adachi, K., Chung, S. H., and Buseck, P.R., 2010: Shapes of soot aerosol particles and implications for their effects on climate. *Journal of Geophysical Research*, **115**, D15206.

Bi, L., P. Yang, G. W. Kattawar, and M. I. Mishchenko, 2013. Efficient implementation of the invariant imbedding T-matrix method and the separation of variables method applied to large nonspherical inhomogeneous particles. *Journal of Quantitative Spectroscopy and Radiative Transfer*.

Bi, L. and P. Yang, 2014: Accurate simulation of the optical properties of Atmospheric ice crystals with the invariant imbedding T-matrix method. *Journal of Quantitative Spectroscopy and Radiative Transfer*.

Bi, L., P. Yang, C. Liu, B. Yi, B. A. Baum, B. van Diedenhoven, H. Iwabuchi, 2014: Assessment of the accuracy of the conventional ray-tracing technique: Implications in remote sensing and radiative transfer involving ice clouds. *Journal of Quantitative Spectroscopy & Radiative Transfer* **146** 158–174

Bohren, C. F., Huffman, D. R. 1983: Absorption and Scattering of Light by Small Particles, John Wiley & Sons.

Bond, T., and Bergstrom, 2006: Light absorption by carbonaceous particles: an investigative Review. *Aerosol Science and Technology,* 40:27–67.

Bond, T., and Coauthors, 2013: Bounding the role of black carbon in the climate system: A scientific assessment. *Journal of Geophysical Research: Atmospheres*.

Cappa, C. D., and Coauthors, 2012: Radiative absorption enhancements due to the mixing state of atmospheric black carbon. *Science*, **337,** 1078-1081.

Cappa, C.D., and Coathors, 2013: Response to Comment on "Radiative absorption enhancements due to the mixing state of atmospheric black carbon". Science **339**, 393.

Chen, H., M. Iskander, and J. Penner, 1990: Light scattering and absorption by fractal agglomerates and coagulations of smoke aerosols. *Journal of Modern Optics*, **37,** 171-181.

Chylek, P., and James A. Coakley, Jr., 1974: Aerosols and Climate." *Science* **183**: 75-77.

Chýlek, P., Videen, G., Geldart, D., Dobbie, J. S., and Tso, H., 2000: Effective medium approximations for heterogeneous particles. *Light Scattering by Nonspherical Particles: Theory, Measurements, and Applications*, **1,** 274.

Davis, P. J., and P. Rabinowitz, 2007: *Methods of numerical integration.* Courier Dover Publications.

Della Sala, F., and S. D'Agostino, 2013: *Handbook of Molecular Plasmonics.* CRC Press.

Draine, B. T., 1988: The discrete-dipole approximation and its application to interstellar graphite grains. *The Astrophysical Journal*, **333,** 848-872.

——, 2000: The discrete dipole approximation for light scattering by irregular targets. *Light Scattering by Nonspherical Particles: Theory, Measurements, and Applications*, **1,** 131.

Flanner, M., X. Liu, C. Zhou, J. E. Penner, and C. Jiao, 2012: Enhanced solar energy absorption by internally-mixed black carbon in snow grains. *Atmospheric Chemistry and Physics*, **12,** 4699-4721.

Fornea, A. P., S. D. Brooks, J. B. Dooley, and A. Saha, 2009: Heterogeneous freezing of ice on atmospheric aerosols containing ash, soot, and soil, Journal Of Geophysical Research-Atmospheres, 114.

Fu, Q., 2007: A new parameterization of an asymmetry factor of cirrus clouds for climate models. *Journal of the Atmospheric Sciences*, **64,** 4140-4150.

Fuller, K. A.,1995: Scattering and absorption cross sections of compounded spheres, III, Spheres containing arbitrarily located spherical inhomogeneities, *J. Opt. Soc. Am. A*, **12,** 893-904.

Garnett, J. M., 1906: Colours in metal glasses, in metallic films, and in metallic solutions. II. *Philosophical Transactions of the Royal Society of London. Series A, Containing Papers of a Mathematical or Physical Character*, 237-288.

Geogdzhayev, I. and Diedenhoven, B., 2016: The effect of roughness model on scattering properties of ice crystals. J*ournal of Quantitative Spectroscopy and Radiative Transfer*, **178**, 134-141.

Ghan, S. J., and S. E. Schwartz, 2007: Aerosol properties and processes: A path from field and laboratory measurements to global climate models. *Bulletin of the American Meteorological Society*, **88,** 1059-1083.

Ghan, S. J., Liu,X., Easter, R. C., Zaveri R., Rasch P. J., and Yoon, J.-H. 2012: Toward a Minimal Representation of Aerosols in Climate Models: Comparative Decomposition of Aerosol Direct, Semidirect, and Indirect Radiative Forcing. *Journal of climate*, **25,** 6461-6476.

Glen A. and Brooks, S. D., 2013: A new method for measuring optical scattering properties of atmospherically relevant dusts using the Cloud and Aerosol Spectrometer with Polarization (CASPOL). *Atmos. Chem. Phys.*, **13**, 1–12.

Glen A. and Brooks, S. D., 2014, Single particle measurements of the optical properties of small ice crystals and heterogeneous ice nuclei Aerosol Science and Technology **48**(11), 1123-1132.

Grenfell, T. C., S. P. Neshyba, and S. G. Warren, 2005: Representation of a nonspherical ice particle by a collection of independent spheres for scattering and absorption of radiation: 3. Hollow columns and plates. *Journal of Geophysical Research: Atmospheres (1984–2012)*, **110**.

Heymsfield, A. J., and J. Iaquinta, 2000: Cirrus crystal terminal velocities. *Journal of the Atmospheric Sciences*, **57,** 916-938.

Hong, G., and P. Minnis (2015), Effects of spherical inclusions on scattering propertiesof small ice cloud particles, J. Geophys. Res. Atmos., 120, 2951–2969, doi:10.1002/2014JD022494.

Hoose, C., and O. Mohler, 2012: Heterogeneous ice nucleation on atmospheric aerosols: A review of the results from laboratory expeirments, Atmos. Chem. Phys., 12, 9817-9854, doi:doi:10/5194/acp-12-9817-2012.

Ishimoto, H., K. Masuda, Y. Mano, N. Orikasa, A. Uchiyama, 2012: Irregularly shaped ice aggregates in optical modeling of convectively generated ice clouds. *Journal of Quantitative Spectroscopy & Radiative Transfer* **113** 632-643.

Jacobson, M. Z., 2006: Effects of externally-through-internally-mixed soot inclusions within clouds and precipitation on global climate. Journal of Physical Chemistry A **110**, 6860-6873.

Jacobson, M. Z., 2012: Investigating cloud absorption effects: Global absorption properties of black carbon, tar balls, and soil dust in clouds and aerosols. *Journal of Geophysical Research*, **117** doi:10.1029/2011JD017218 201.

Kaufman, Y., and Coauthors, 1994: Size distribution and scattering phase function of aerosol particles retrieved from sky brightness measurements. *Journal of Geophysical Research: Atmospheres (1984–2012)*, **99,** 10341-10356.

Kinne, S., and Coauthors, 1997: Cirrus cloud radiative and microphysical properties from ground observations and in situ measurements during FIRE 1991 and their application to exhibit problems in cirrus solar radiative transfer modeling. *Journal of the atmospheric sciences*, **54,** 2320-2344.

Kokhanovsky, A. A., 2013: *Light Scattering Reviews 8: Radiative transfer and light scattering.* Springer Science & Business.

Korolev, A., G. Isaac, and Hallett, J., 1999: Ice particle habits in Arctic clouds. *Geophysical research letters*, **99,** 1299-1302.

Lahaye, J., and F. Ehrburger-Dolle, 1994: Mechanisms of carbon black formation. Correlation with the morphology of aggregates. *Carbon*, **32,** 1319-1324.

Lee, Y.-K., and Coauthors, 2003: Use of circular cylinders as surrogates for hexagonal pristine ice crystals in scattering calculations at infrared wavelengths. *Applied optics*, **42,** 2653-2664.

Liu, L., and M. I. Mishchenko, 2007: Scattering and radiative properties of complex soot and soot-containing aggregate particles. *Journal of Quantitative Spectroscopy and Radiative Transfer*, **106,** 262-273.

Macke, A., P. N. Francis, G. M. McFarquhar, and S. Kinne, 1998: The role of ice particle shapes and size distributions in the single scattering properties of cirrus clouds. *Journal of the atmospheric sciences*, **55,** 2874-2883.

Mishchenko, M. I., and K. Sassen, 1998: Depolarization of lidar returns by small ice crystals: An application to contrails. *Geophysical Research Letters*, **25,** 309-312.

Mishchenko, M. I., and Macke, M. 1999: How big should hexagonal ice crystals be to produce halos? *Appl. Opt.* **38**:1626-9.

Mishchenko, M.I., Travis, L.D. and Lacis, A.A., 2002. Scattering, absorption, and emission of light by small particles. Cambridge university press.

Muinonen, K., Nousiainen, T., Lindqvist, H., Muñoz, O., Videen, G. 2009: Light scattering by Gaussian particles with internal inclusions and roughened surfaces using ray optics. *Journal of Quantitative Spectroscopy & Radiative Transfer* **110**, 1628–1639.

Murray, B. J., D. O'Sullivan, J. D. Atkinson, and M. E. Webb, 2012: Ice nucleation by particles immersed in supercooled cloud droplets, Chem. Soc. Rev, 41, 6519-6554.

Neshyba, S. P., T. C. Grenfell, and S. G. Warren, 2003: Representation of a nonspherical ice particle by a collection of independent spheres for scattering and absorption of radiation: 2. Hexagonal columns and plates. *Journal of geophysical research*, **108,** 4448.

Nicolet, M., M. Schnaiter, and O. Stetzer, 2012: Circular depolarization ratios of single water droplets and finite ice circular cylinders: a modeling study. *Atmospheric Chemistry and Physics*, **12,** 4207-4214.

Nousiainen T, Muinonen K, Avelin J, Sihvola A., 2001: Microwave backscattering by nonspherical ice particles at 5.6 GHz using second-order perturbation series. *Journal of Quantitative Spectroscopy Radiation Transfer*, **70**, 639-61.

Nousiainen, T., 2009. Optical modeling of mineral dust particles: A review. *Journal of Quantitative Spectroscopy and Radiative Transfer*, **110,** 1261-1279.

Penttilä, A., and Coauthors, 2007: Comparison between discrete dipole implementations and exact techniques. *Journal of Quantitative Spectroscopy and Radiative Transfer*, **106,** 417-436.

Penttilä, A. and K. Lumme, 2011: Optimal cubature on the sphere and other orientation averaging schemes, J. Quant. Spectrosc. Radiat. Transfer 112, 1741-1746 (2011).

Ramanathan, V. and G. Carmichael, 2008: Global and regional climate changes due to black carbon. *Nature geoscience*, **1,** 221-227.

Santoro, R., H. Semerjian, and R. Dobbins (1983), Soot particle measurements in diffusion flames, *Combust. Flame*, **51**, 203-218.

Schmitt, C. G. and A. J.Heymsfield, 2010: The Dimensional Characteristics of Ice Crystal Aggregates from Fractal Geometry. J. Atmos. Sci., **67,** 1605-1616.

Schwarz, J., and Coauthors, 2006: Single-particle measurements of midlatitude black carbon and light-scattering aerosols from the boundary layer to the lower stratosphere. *Journal of Geophysical Research: Atmospheres (1984–2012)*, **111**.

Sorensen, C., 2001: Light scattering by fractal aggregates: a review. *Aerosol Science & Technology*, **35,** 648-687.

Yang, P., and Q. Fu, 2009: Dependence of ice crystal optical properties on particle aspect ratio. *Journal of Quantitative Spectroscopy and Radiative Transfer*, **110,** 1604-1614.

Yang, P., L. Bi, B. A. Baum, K.-N. Liou, G. W. Kattawar, M. I. Mishchenko, and B. Cole, 2013: Spectrally Consistent Scattering, Absorption, and Polarization Properties of Atmospheric Ice Crystals at Wavelengths from 0.2 to 100 μ m. *Journal of the Atmospheric Sciences*, **70,** 330-347.

Yurkin, M. A., and A. G. Hoekstra, 2007: The discrete dipole approximation: an overview and recent developments. *Journal of Quantitative Spectroscopy and Radiative Transfer*, **106,** 558-589.

——, 2013: User manual for the discrete dipole approximation code ADDA 1.2.

Yurkin, M. A., V. P. Maltsev, and A. G. Hoekstra, 2007: The discrete dipole approximation for simulation of light scattering by particles much larger than the wavelength. *Journal of Quantitative Spectroscopy and Radiative Transfer*, **106,** 546-557.